










# Spatially Resolved Outflows in a Seyfert Galaxy at $z = 2.39$

Travis C. Fischer<sup>1,2,12</sup> , J. R. Rigby<sup>1</sup>, G. Mahler<sup>3</sup> , M. Gladders<sup>4,5</sup>, K. Sharon<sup>3</sup> , M. Florian<sup>1</sup> , S. Kraemer<sup>2</sup>, M. Bayliss<sup>6</sup> ,  
H. Dahle<sup>7</sup> , L. Felipe Barrientos<sup>8</sup>, S. Lopez<sup>9</sup>, N. Tejos<sup>10</sup>, T. Johnson<sup>3</sup>, and E. Wuyts<sup>11</sup> 

<sup>1</sup>Observational Cosmology Lab, Goddard Space Flight Center, Code 665, Greenbelt, MD 20771, USA; [travis.c.fischer@nasa.gov](mailto:travis.c.fischer@nasa.gov)

<sup>2</sup>Institute for Astrophysics and Computational Sciences, Department of Physics, The Catholic University of America, Washington, DC 20064, USA

<sup>3</sup>Department of Astronomy, University of Michigan, 500 Church Street, Ann Arbor, MI 48109, USA

<sup>4</sup>Department of Astronomy & Astrophysics, University of Chicago, 5640 South Ellis Avenue, Chicago, IL 60637, USA

<sup>5</sup>Kavli Institute for Cosmological Physics, University of Chicago, 5640 South Ellis Avenue, Chicago, IL 60637, USA

<sup>6</sup>MIT Kavli Institute for Astrophysics and Space Research, 77 Massachusetts Avenue, Cambridge, MA 02139, USA

<sup>7</sup>Institute of Theoretical Astrophysics, University of Oslo, PO Box 1029, Blindern, NO-0315 Oslo, Norway

<sup>8</sup>Instituto de Astrofísica, Pontificia Universidad Católica de Chile, Vicuña Mackenna 4890, Santiago, Chile

<sup>9</sup>Departamento de Astronomía, Universidad de Chile, Casilla 36-D, Santiago, Chile

<sup>10</sup>Instituto de Física, Pontificia Universidad Católica de Valparaíso, Casilla 4059, Valparaíso, Chile

<sup>11</sup>ArmenTeKort, Antwerp, Belgium

Received 2018 November 8; revised 2019 March 12; accepted 2019 March 19; published 2019 April 22

## Abstract

We present the first spatially resolved analysis of rest-frame optical and UV imaging and spectroscopy for a lensed galaxy at  $z = 2.39$  hosting a Seyfert active galactic nucleus (AGN). Proximity to a natural guide star has enabled observations with high signal-to-noise ratio using Very Large Telescope SINFONI + adaptive optics (AO) of rest-frame optical diagnostic emission lines, which exhibit an underlying broad component with full width at half maximum  $\sim 700 \text{ km s}^{-1}$  in both the Balmer and forbidden lines. Measured line ratios place the outflow robustly in the region of the ionization diagnostic diagrams associated with AGNs. This unique opportunity—combining gravitational lensing, AO guiding, redshift, and AGN activity—allows for a magnified view of two main tracers of the physical conditions and structure of the interstellar medium in a star-forming galaxy hosting a weak AGN at Cosmic Noon. By analyzing the spatial extent and morphology of the  $\text{Ly}\alpha$  and dust-corrected  $\text{H}\alpha$  emission, disentangling the effects of star formation and AGN ionization on each tracer, and comparing the AGN-induced mass outflow rate to the host star formation rate, we find that the AGN does not significantly impact the star formation within its host galaxy.

*Key words:* galaxies: active – galaxies: Seyfert – galaxies: star formation – gravitational lensing: strong

## 1. Introduction

Galaxies at the peak of cosmic star formation live in a state of punctuated equilibrium, where continuous accretion of gas from the cosmic web feeds large molecular gas reservoirs, and is balanced by star formation and outflows. Galactic wind feedback is widely acknowledged to play a critical role in the evolution of galaxies by expelling gas from their central regions, shutting down their global star formation, and regulating their stellar mass and growth in size (Davé et al. 2012; Vogelsberger et al. 2013). However, the physical mechanisms involved and the relative importance of active galactic nuclei (AGNs) and star formation as the main feedback drivers remain poorly understood. AGN-driven feedback is evident in luminous but rare QSOs and radio galaxies, but observational evidence is lacking for AGN feedback in less extreme, normal star-forming galaxies (SFGs) (Fabian 2012). In optical and infrared spectroscopy, evidence of AGN outflows, which can produce feedback, is observed as relatively broad emission lines, with  $\text{FWHM} > 250 \text{ km s}^{-1}$ , inside the narrow-line region (NLR), a region of relatively low-density ionized gas extending from the nuclear torus to distances of hundreds to thousands of parsecs from the nucleus.

Recent studies by Fischer et al. (2017, 2018) find that outflows may not be powerful enough in nearby AGNs to drive gas out to bulge-radius distances of 2–3 kpc. Kinematics within the NLR are largely due to rotation and in situ acceleration of

material originating in the host disk. Spatially resolved outflowing gas in Type 2 Seyferts and nearby ( $z < 0.12$ ) QSOs extends to a fraction of radii typical of host-galaxy stellar bulges ( $r \sim 2\text{--}3 \text{ kpc}$ ). These findings suggest that outflows at  $z \sim 0$  may not be powerful enough to evacuate gas from their entire bulges. Several other studies have reached similar conclusions (Karouzos et al. 2016; Villar-Martín et al. 2016; Keel et al. 2017; Ramos Almeida et al. 2017).

Förster Schreiber et al. (2014) and Genzel et al. (2014) have reported evidence for likely AGN-driven outflows in the central regions of massive ( $\log(M_*/M_\odot) \geq 10.9$ ) main-sequence SFGs at high redshifts ( $z \sim 2$ ) with  $\text{FWHM} \sim 1000\text{--}1500 \text{ km s}^{-1}$  and elevated  $[\text{N II}]/\text{H}\alpha$  ratios  $\geq 0.5$ . The outflows are resolved over the inner 2–3 kpc of the galaxies and detected in the forbidden  $[\text{N II}]$  and  $[\text{S II}]$  lines as well as in  $\text{H}\alpha$ . Therefore, these broad emission lines cannot be due only to a virialized, parsec-scale AGN broad-line region. The mass outflow rates are estimated to be comparable to or exceed the star formation rate (SFR) of the galaxy, thus creating an important avenue for the quenching of star formation. The next step is to measure the size, geometry, velocity profile, and mass loading through high-resolution mapping of an outflow region. However, restrictions on sensitivity and spatial resolution currently limit us to barely resolving ionized-gas structures in only a few of the largest and most massive SFGs at  $z \sim 2$ .

Our team has recently discovered a bright, lensed galaxy, SGAS J003341.5+024217, henceforth SGAS 0033+02 (Figure 1), as described in the Magellan Evolution of Galaxies Spectroscopic and

<sup>12</sup> James Webb Space Telescope NASA Postdoctoral Program Fellow.



**Figure 1.** *HST*/WFC3 F555W/F814W/F105W composite image of the lensed galaxy SGAS J003341.5+024217. The galaxy is multiply imaged as an elongated arc and two counter images. Fields of view for SINFONI *H*- and *K*-band observations of the arc are represented by blue and red boxes, respectively. The bright source to the southeast is a star, which was used as the natural guide star for SINFONI adaptive optics.

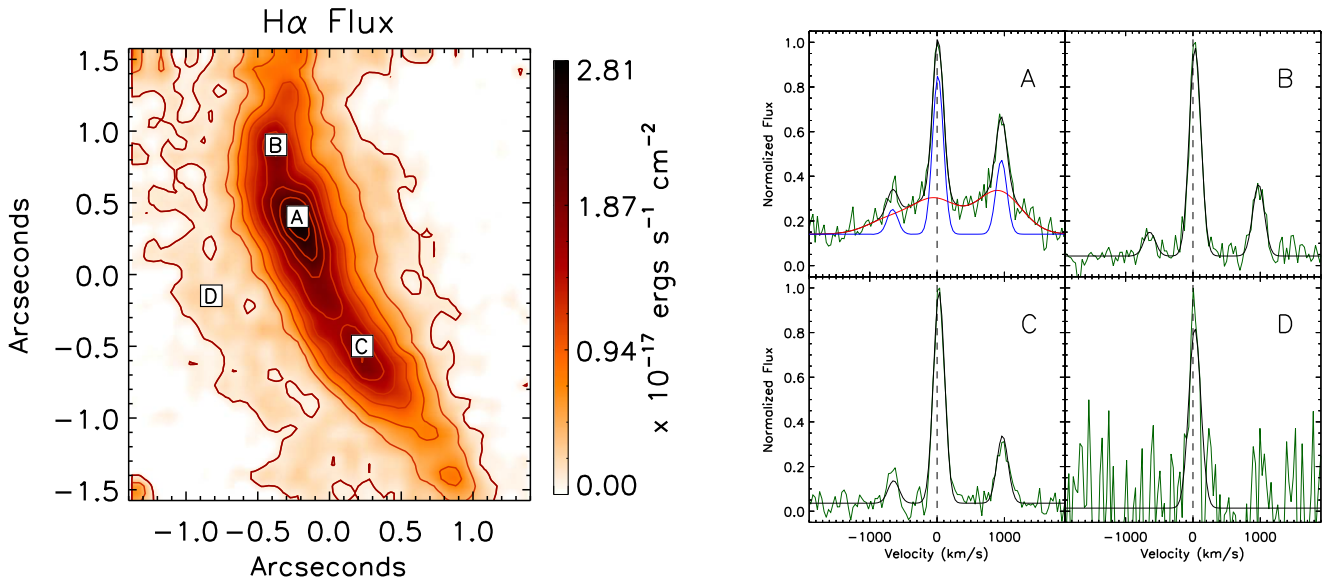


**Figure 2.** Left: continuum-subtracted  $H\alpha$  flux distribution in SGAS 0033+02 obtained from the combined VLT/SINFONI  $\sim 3'' \times 3''$  *K*-band IFU data cube, smoothed with a Gaussian of  $\text{FWHM} = 2.0 \times 2.0$  pixels. Outer, dark red contours represent a lower flux limit of  $3\sigma$  signal-to-noise ratio. Right: spectra of individual spaxels sampling four  $H\alpha$  regions, each overplotted with their best fitting model, with approximate spaxel positions labeled in the  $H\alpha$  image. The solid black line represents the total model. Blue and red lines represent  $H\alpha + [\text{N II}] \lambda\lambda 6548, 6583$  narrow and wide Gaussian components, respectively. The vertical dashed black line represents the  $H\alpha \lambda 6563$  wavelength at systemic velocity.

Ultraviolet Reference Atlas (Rigby et al. 2018), that offers a unique opportunity to spatially resolve the influence of AGN feedback in a galaxy residing near Cosmic Noon at  $z \sim 2.4$ .

SGAS 0033+02 was identified as a candidate lensed system through the Sloan Giant Arcs Survey (M. Gladders et al. 2019, in preparation), in which objects with arc-like morphology are identified along lines of sight with photometric evidence for cluster- or group-scale masses, via a direct visual examination of Sloan Digital Sky Survey imaging data. Follow-up *gri*

imaging acquired with the MOSCA imager on the 2.5 m Nordic Optical Telescope on UT 2012 September 15 confirmed the arc-like morphology of this system, and a spectroscopic redshift of  $z = 2.378$  was obtained with the same telescope using the ALFOSC spectrograph on the Nordic Optical Telescope on UT 2013 September 1.

Fortuitously, a bright ( $g \sim 15.4$ ) star appears in projection only  $7''$  from the main image of the lensed arc SGAS 0033+02. Recognizing this, we obtained laser adaptive optics (AO)

observations using this guide star with the SINFONI instrument on the Very Large Telescope (VLT).

VLT/SINFONI integral field unit (IFU) observations of outflows in luminous AGNs at  $1.5 < z < 3$  have been resolved in detail in previous studies (Nesvadba et al. 2008, 2011, 2017; Carniani et al. 2015; Cresci et al. 2015; Perna et al. 2015; Brusa et al. 2016; Förster Schreiber et al. 2018). However, through the combination of observations across several observatories, we are able to spatially resolve the size, geometry, and mass loading of AGN outflows on scales of tens of parsecs for the first time at high redshift.

## 2. Observations and Data Reduction

### 2.1. Hubble Space Telescope (HST) WFC3 Imaging Observations

Imaging of SGAS 0033+02 was acquired using the *HST* Wide Field Camera 3 during two visits on 2016 October 30 and November 8. In the IR channel, images were taken in the F140W and F105W filters with cumulative exposure times of 459 s and 1026 s respectively. In the UVIS channel, exposures were taken in the F410M, F814W, and F555W filters with cumulative exposure times of 7256 s, 1900 s, and 1748 s respectively. At the redshift of the source,  $z = 2.39$ , these filters provide a wide wavelength coverage, but isolate Ly $\alpha$  emission entirely within the F410M filter.

The *HST* imaging data were reduced using the software package, DrizzlePac.<sup>13</sup> Images were aligned using tweakreg, then drizzled, using astrodrizzle, to a common reference grid with a scale of 0.03 arcsec/pixel, with a Gaussian kernel and a drop size of 0.8. Three hot pixels in the IR channel near or within the main arc consistently failed to flag in astrodrizzle, resulting in artifacts in the final data products that could easily be mistaken for real substructure within the arc. These hot pixels were flagged manually in the data quality extension of the flat-field calibrated files before creating the final drizzled images, and thus the final data products are free from these artifacts.

Continuum-subtracted Ly $\alpha$  imaging was produced using the F410M medium-band filter, with the F555W filter providing the continuum flux. Given the high equivalent width of Ly $\alpha$  in the MagE spectrum described below,  $EW_{\text{obs}} = 203 \text{ \AA}$ , and the F410M bandpass of  $70 \text{ \AA}$ , we calculate that Ly $\alpha$  contributes 74% of the flux in F410M, with the remainder coming from continuum. We then scale the F555W image to match that continuum level, using annular aperture photometry of SGAS 0033+02 in the F410M and F555W *HST* images, covering the same region as the MagE aperture.

### 2.2. MagE Magellan Observations

Observations of SGAS 0033+02 were obtained with the MagE instrument on the Magellan Baade telescope on UT 2015 November 7 and 10, for a total of 7 hr of integration. The spectra cover observed wavelengths of 3200–8280  $\text{\AA}$ , including Ly $\alpha$ . A description of the observations and data reduction, and the MagE spectra themselves, were published by Rigby et al. (2018). Their Figure 1 shows that over the course of the observations, the  $2 \times 10$  MagE slit covered the full extent of the SGAS 0033+02 arc.

### 2.3. VLT SINFONI and MUSE IFU Observations

Observations of SGAS 0033+02 using VLT/SINFONI+AO were taken across several nights (2015 September 8, October 10, and December 4, 6, 9, and 12) in the *H*- and *K*-bands, with resolving powers of  $R = \lambda/\delta\lambda = 3000$  and 4000 and covering the spectral regions 1.45–1.85 and 1.95–2.45  $\mu\text{m}$  respectively, with a pixel scale  $0''.05 \times 0''.1$  and sampling a field of view of  $3''.2 \times 3''.2$ . Observations were carried out in observing blocks (OBs) of an OSOOSO pattern, alternating object (O) and sky (S) positions. Each OB was dithered by  $0''.15$  around the central position to mitigate bad pixels and cosmic rays. Eight individual exposures of 600 s were obtained in the *H*-band and 28 individual exposures of 600 s in the *K*-band, for totals of 1 hr 20 minutes and 4 hr 40 minutes of on-source integration, respectively. VLT/SINFONI data were reduced using the software package SPRED developed specifically for SPIFFI (Schreiber et al. 2004; Abuter et al. 2006) following the procedures described in Förster Schreiber et al. (2009). The offsets between individual cubes were determined from the known dither pattern within each OB, and the location of the acquisition star observed before each OB. The final point-spread function (PSF) is created by fitting a circularly symmetric 2D Gaussian profile to acquisition star exposures taken prior to each OB of the science target, and results in FWHMs of 0.19 in the *K*-band and 0.18 in the *H*-band. The PSF FWHMs correspond to the effective resolution of all observations for our target. Early B-type standard stars were observed each night to provide flux calibration and telluric correction. Figure 2 shows a continuum-subtracted H $\alpha$  flux map from the *K*-band field of view, with representative spectra from various observed emission-line knots.

Observations of SGAS 0033+02 using VLT/MUSE were obtained under the program 098.A-0459(A). The 1 arcmin field of view is sampled with  $349 \times 352 0''.2$  wide spaxels. Our setup provided a wavelength range from 4650 to 9300  $\text{\AA}$  at a resolving power  $R$  ranging from 2000 to 4000. Each spectral bin is 1.25  $\text{\AA}$  wide. The observations were carried out in service mode during dark time, with clear-sky conditions, airmass below 1.8, and seeing better than  $0''.7$  on the nights of 2017 September 19 and 20. We obtained a total of 12 exposures of 700 s on-target each. The exposures were taken within OBs of four exposures each. We applied a small dithering and  $90^\circ$  rotations between exposures to reject cosmic rays and minimize patterns of the slicers on the processed combined cube. We reduced all the observations using the MUSE pipeline recipe v1.6.4 and ESO reflex v2.8.5. The individual exposures were combined into one final science data cube. The total on-target time was therefore 2.3 hr. The sky subtraction was improved on this cube using the Zurich Atmospheric Purge algorithm v1.0.

## 3. Image-plane Analysis

### 3.1. SINFONI Spectroscopic Fitting

Emission-line kinematics and fluxes of H $\alpha$ , [N II], [O III], and H $\beta$  were measured in each spaxel of our SINFONI *H*- and *K*-band data cubes by fitting Gaussians in an automated routine. Our fitting process, previously discussed in depth in Fischer et al. (2017), uses the Importance Nested Sampling algorithm as implemented in the MultiNest library (Feroz & Hobson 2008; Feroz et al. 2009, 2013; Buchner et al. 2014) to compute the logarithm of the evidence,  $\ln Z$ , for models containing a continuum plus zero to three Gaussian components per emission line. Gaussians were defined using Gaussian

<sup>13</sup> drizzlepac.stsci.edu



parameters  $\mu$  (centroid),  $\sigma$  (dispersion), and  $H$  (peak height). When comparing two models, i.e., a model with zero Gaussians ( $M_0$ ) and a model with one Gaussian ( $M_1$ ), the simpler model is chosen unless the more complex model,  $M_1$ , has a significantly better evidence value,  $|\ln(Z_1/Z_0)| > 5$  (99% more likely). Fits of emission lines in individual spaxels used different models for each band.  $H$ -band models first measured [O III]  $\lambda 5007$ , simultaneously fitting a second set of components to [O III]  $\lambda 4959$  in order to properly account for flux contributions from wing emission between the two lines, and then tested for the presence of  $H\beta$ . Gaussian wavelength centroid and dispersion parameters of [O III]  $\lambda 4959$  components were fixed following parameters used in fitting [O III]  $\lambda 5007$  components, with the flux of [O III]  $\lambda 4959$  fixed to be one-third that of the [O III]  $\lambda 5007$  flux. Gaussian wavelength centroid and dispersion parameters of  $H\beta$  components were fixed in the same manner, because we assume that the lines originate from the same emission region, and the  $H\beta$  flux was left as a free parameter.  $K$ -band models first measured  $H\alpha$  and then tested for the presence of [N II]  $\lambda\lambda 6548, 6584$ . Gaussian wavelength centroid and dispersion parameters of [N II]  $\lambda\lambda 6548, 6584$  were also fixed following parameters used in fitting  $H\alpha$ , again under the assumption that the lines originate from the same emission region, with the flux of [N II]  $\lambda 6548$  fixed to be one-third that of the [N II]  $\lambda 6584$  flux, which was left as a free parameter.

Initial input parameters in our models are selected based on physical considerations. The centroid position for each Gaussian was limited to a  $40 \text{ \AA}$  range around the wavelength that contained the entirety of the line profiles throughout each data cube. Gaussian standard deviation ranged from the spectral resolution of the  $H$ - and  $K$ -band gratings to an artificial FWHM limit of  $\sim 800 \text{ km s}^{-1}$ . Gaussian height was defined to allow for an integrated flux that ranged from a  $3\sigma$  detection to a maximum integrated flux of  $3\sigma \times 10^4$ .

Fits from the  $H$ - and  $K$ -band observations are mapped in Figure 3. Observed velocity, FWHM, and integrated fluxes are shown for  $H\alpha$  and [O III]  $\lambda 5007$ , with additional integrated fluxes for  $H\beta$  and [N II], because their velocity and FWHM measurements are identical to [O III] and  $H\alpha$ , respectively. Doppler-shifted velocities are given in the rest frame of the galaxy using air rest wavelengths of each line. We found emission lines present in most spaxels to be best fit with a single Gaussian, with  $H\alpha$  and [N II] emission lines containing two-component line profiles in spaxels surrounding the  $K$ -band continuum peak (shown as a cross in each map of Figure 3) of the lensed galaxy arc. Two-component fits are sorted by FWHM into separate  $H\alpha$ /[N II] maps in Figure 3. Component blending due to lower signal-to-noise ratios for the broad component is observed in regions between fits with different numbers of components, because a jump in line dispersion is observed in the narrow-component FWHM plot at the border between single- and double-component fits.

We find that a majority of the emission-line gas fit with single components, or the narrower of two components, is near systemic velocity or slightly redshifted. Emission-line knots north and south of the continuum peak show symmetric redshifted kinematics. Additional faint filaments observed in  $H\alpha$  and [O III] east and west of the continuum peak also show symmetric redshifted velocities. The broad  $H\alpha$  and [N II] emission-line components over the continuum peak are typically blueshifted, with an average FWHM of  $\sim 540 \text{ km s}^{-1}$  and maximum and average offsets of  $\sim -140 \text{ km s}^{-1}$  and  $\sim -40 \text{ km s}^{-1}$ , respectively. We measure the

spatially resolved maximum extent of the broad-FWHM, blue-shifted gas in the image plane by fitting the region with an ellipse of  $r_{\text{maj}} = 0''.35$ ,  $b/a = 0.4$ , and  $\text{PA} = 30^\circ$  east of north. At  $7''$  from the guide star, we note that a degradation of the reported  $K$ -band PSF is expected, with the Strehl ratio of observations for SGAS 0033+02 decreasing by approximately 20% according to the SINFONI User Manual. Temporal variations of the atmosphere also add uncertainty to the effective PSF during the observations, with individual exposures of PSF stars in similar observations by Förster Schreiber et al. (2018) indicating typical OB-to-OB variations of  $\sim 30\%$  in PSF FWHM. As such, assuming an effective PSF during the observations to be  $\sim 0''.3$ , the spatial extent of the observed outflows remains well resolved.

### 3.2. Ionization Source Diagnostics

We compare measured line flux ratios in an ionization diagnostic diagram (i.e., a BPT diagram, named for Baldwin et al. 1981) to spatially resolve the source of ionization throughout the image-plane arc and determine whether the observed blueshifted outflows can be attributed to an AGN. Note that measured ratios are not affected by magnification because lensing effects are achromatic. To account for the high redshift of our target, we used a redshift-dependent classification that utilizes the standard optical diagnostic line ratios [O III]/ $H\beta$  versus [N II]/ $H\alpha$  as detailed in Kewley et al. (2013). Our initial diagnostic diagram, provided in the left plot in Figure 4, compares line ratios using the integrated flux across all components of each line. Gray points in this distribution have single-component fits for each emission line, while red points use summed fluxes of  $H\alpha$  and [N II]  $\lambda 6584$  emission lines across both a narrow component and a broad one. Decomposing these two-component emission lines into individual narrow and broad components to obtain their individual ratios, as shown in the right plot of Figure 4, we find that the narrow components align with the gray points of the left figure, and that the broad components exhibit an [N II]/ $H\alpha$  ratio that suggests AGN ionization. Note that the position of the broad components on the diagram uses the same [O III]/ $H\beta$  ratio as their corresponding narrow lines because broad [O III]/ $H\beta$  components are not observed in individual spaxels.

In order to detect broad-component signatures of [O III] and  $H\beta$ , we binned spectra over a  $0''.5 \times 0''.5$  square surrounding the continuum peak and a majority of the blueshifted outflows (the binned region is shown in the broad-component  $H\alpha$  and [N II] maps of Figure 3). Fits to the resultant  $H$ - and  $K$ -band spectra are shown in Figure 5, where we are able to detect a broad emission line for [O III], as well as emission from [O I]  $\lambda 6300$  and [S II]  $\lambda\lambda 6716, 6731$ , but remain unable to detect broad  $H\beta$ . Fit parameters for each emission line in the image-plane binned spectra are provided in Table 1. To determine a lower limit to the summed broad-component [O III]/ $H\beta$  ratio, we estimate the flux of the unobserved  $H\beta$  broad component to scale to its narrow component in a similar fashion to the observed broad and narrow components of  $H\alpha$  in the same binned region. The estimated flux of  $3.34 \times 10^{-16} \text{ erg s}^{-1} \text{ cm}^{-2}$  is consistent with our measurements, such that the broad  $H\beta$  would likely be undetectable compared to the low signal of the brighter [O III]  $\lambda 4959$  broad component.

Flux ratios derived from our binned spectrum are plotted as larger, filled points in Figure 4, where the red circle and green and blue half-circles represent flux ratios using both components, the narrow component, and the broad component,

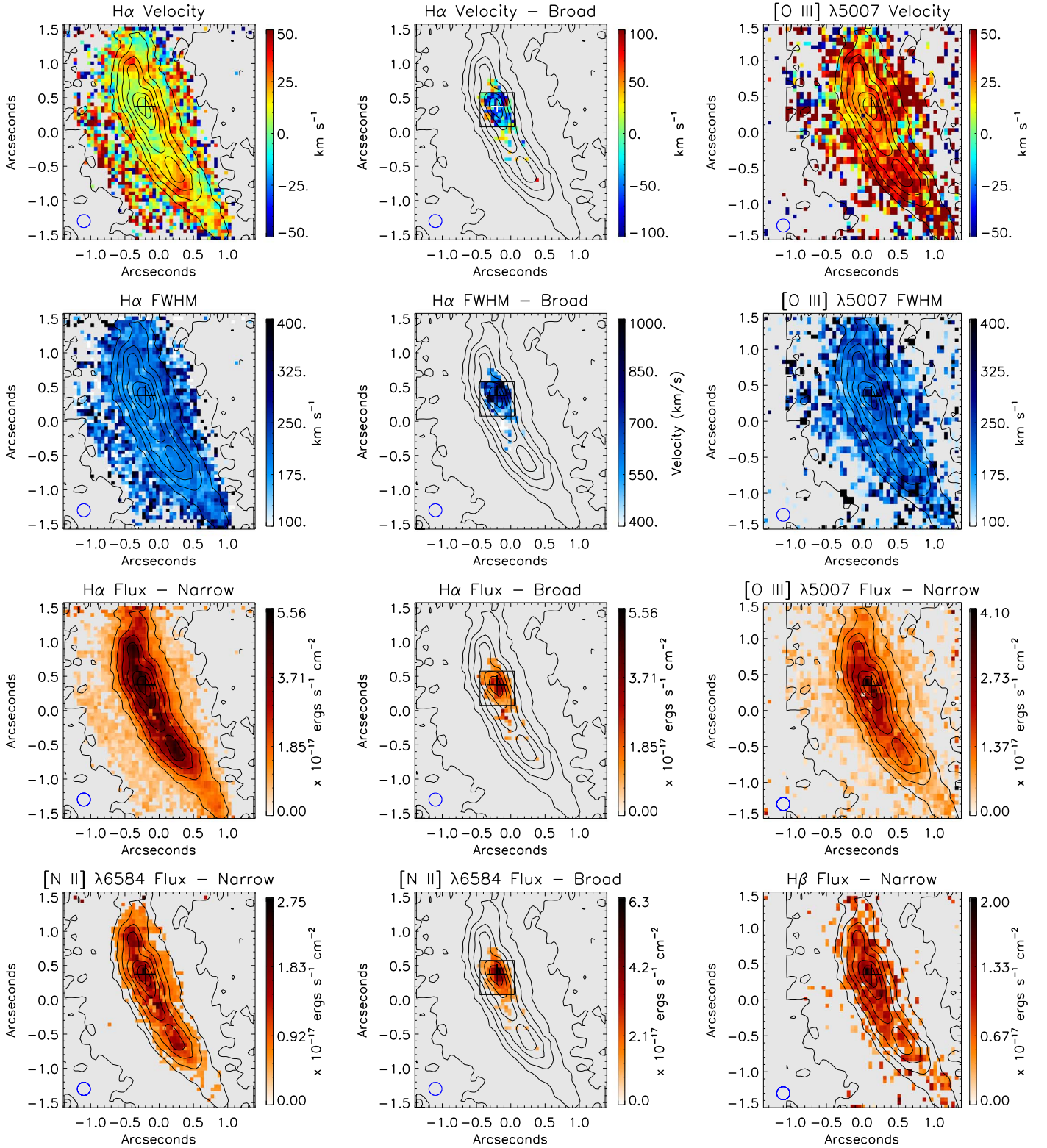


**Figure 3.** SGAS 0033+02 emission line measurements from VLT/SINFONI *H*- and *K*-band IFU observations. The first, second, and third rows display centroid velocity, FWHM, and integrated flux maps, respectively, of H $\alpha$  and [O III]  $\lambda$ 5007 emission-line profiles in the image plane. The fourth row displays integrated flux maps of [N II]  $\lambda$ 6584 and H $\beta$ . H $\alpha$  and [N II] emission-line profiles are separated into narrow and broad components in the left and center columns, respectively. The black boxes in the center column depict a  $0''.5 \times 0''.5$  region over the central outflowing gas, binned to detect broad-component signatures of [O III] and H $\beta$ . Black contours represent integrated, continuum-subtracted H $\alpha$  flux images. The *K*-band (rest-frame optical) continuum flux peak is depicted by a cross.

respectively. We find a lower limit on the broad-component [O III]/H $\beta$  ratio to be 0.54, which is elevated relative to the narrow- and summed-component ratios. This suggests that a

majority of the broad components would likely have larger [O III]/H $\beta$  ratios using their true line fluxes instead of estimates and remain in the AGN-ionized portion of the diagnostic

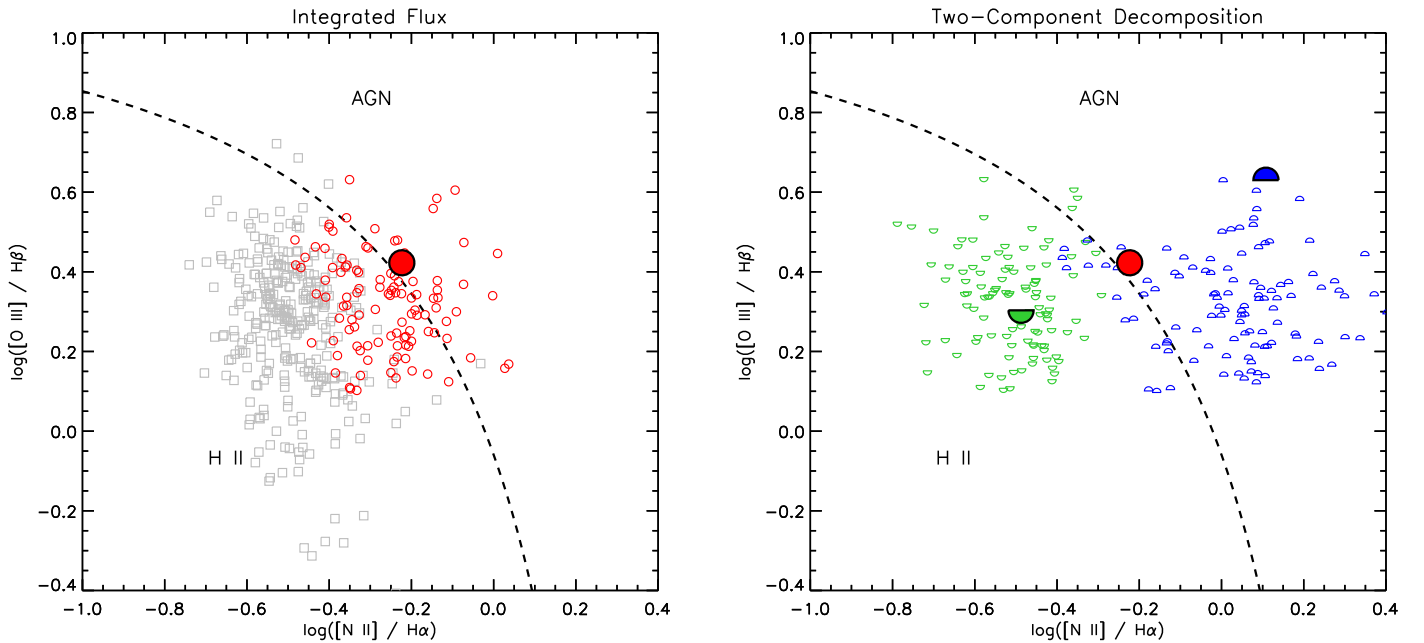


**Figure 4.**  $[\text{N II}]/\text{H}\alpha$  vs.  $[\text{O III}]/\text{H}\beta$  diagnostic diagrams derived from the  $H$ - and  $K$ -band SINFONI observations in the image plane. Left: diagnostic diagram for individual spaxel measurements using the total, integrated flux of each emission line. The division between H II and AGN ionization is defined by the redshift-dependent classification from Kewley et al. (2013). Gray squares represent ratios from spaxels with fluxes measured using a single line component in all measured lines. Red open circles represent ratios from spaxels with fluxes measured using a single line component in  $[\text{O III}]$  and  $\text{H}\beta$  and two components for  $[\text{N II}]$  and  $\text{H}\alpha$ . The red filled circle shows the ratio measured from a binned spectrum containing all spaxels with two emission-line components. Right: diagnostic diagram for individual spaxel measurements with the two-component  $[\text{N II}]$  and  $\text{H}\alpha$  emission lines decomposed into narrow and broad components. Green open lower-half circles represent narrow-component fluxes and blue open upper-half circles represent broad-component fluxes. The red filled circle again shows the ratio measured from a binned spectrum containing all spaxels with two emission-line components, and the filled green lower-half circles and blue open upper-half circles show the ratio measured from the narrow and broad components of the binned spectrum, respectively.

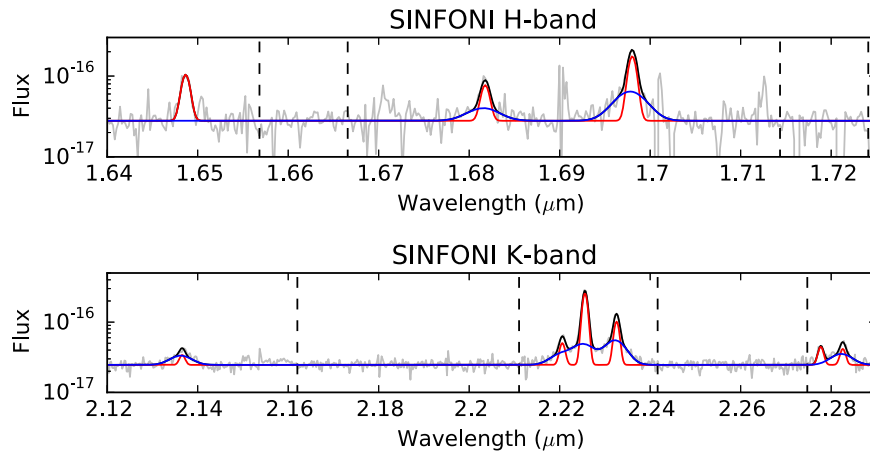


**Figure 5.** Gaussian fits to the binned SINFONI spectrum of the central  $0''.5 \times 0''.5$  region over the lensed image-plane arc continuum peak. Top:  $H$ -band spectrum fitting  $\text{H}\beta$  and  $[\text{O III}]$   $\lambda\lambda 4959, 5007$ . Bottom:  $K$ -band spectrum fitting  $[\text{O I}]$   $\lambda 6300$ ,  $\text{H}\alpha$ ,  $[\text{N II}]$   $\lambda\lambda 6548, 6584$ , and  $[\text{S II}]$   $\lambda\lambda 6716, 6731$ . Gaussian fits to  $[\text{O III}]$   $\lambda 4959$  and  $[\text{N II}]$   $\lambda 6548$  used height parameters fixed to be one-third of  $[\text{O III}]$   $\lambda 5007$  and  $[\text{N II}]$   $\lambda 6584$ , respectively. No broad component is detected for  $\text{H}\beta$  and  $[\text{S II}]$   $\lambda 6716$ . The gray line represents SINFONI spectral data. The solid black line represents the total model. Blue and red lines represent decompositions of broad and narrow Gaussian components, respectively. Flux is in units of  $\text{erg s}^{-1} \text{cm}^{-2} \text{\AA}^{-1}$ .

diagram. In tandem, the measured emission-line flux ratios and kinematics suggest that we are observing outflows from an AGN in the image-plane arc of SGAS 0033+02.

### 3.3. Spatially Resolved $\text{Ly}\alpha$ Structure

We compare the image-plane morphology of the  $\text{H}\alpha$  gas from our SINFONI spectral fits to that of the  $\text{Ly}\alpha$ -emitting gas from  $HST$  imaging, as shown in Figure 6, to determine whether the AGN outflows have some influence on the propagation or

escape of  $\text{Ly}\alpha$  photons. We find that the  $\text{Ly}\alpha$ -emitting gas is most prominent between, rather than cospatial with, the brightest knots of  $\text{H}\alpha$  that reside over the AGN and likely star-forming regions. This discrepancy between the morphology of  $\text{Ly}\alpha$  and  $\text{H}\alpha$  has also been reported in similar studies of local starburst galaxies (Östlin et al. 2009; Hayes et al. 2013) and high-redshift ( $z < 2.5$ ) quasar hosts (Bayliss et al. 2017).

We also compare the spectral signatures of  $\text{Ly}\alpha$  and  $\text{H}\alpha$  in Figure 6, with  $\text{Ly}\alpha$  emission obtained from long-slit MagE observations covering the full spatial extent of the arc as



**Table 1**  
Central  $0''.5 \times 0''.5$  Binned AGN Flux Measurements

Line	FWHM (km s <sup>-1</sup> )	Observed Image Plane (erg s <sup>-1</sup> cm <sup>-2</sup> )	Observed Source Plane (erg s <sup>-1</sup> cm <sup>-2</sup> )	Dereddened Source Plane (erg s <sup>-1</sup> cm <sup>-2</sup> )
<b>Narrow Component</b>				
H $\beta$	190	$(8.77 \pm 2.68) \times 10^{-16}$	$(2.80 \pm 1.04) \times 10^{-18}$	$(6.94 \pm 2.58) \times 10^{-18}$
[O III] $\lambda$ 5007	190	$(1.70 \pm 0.49) \times 10^{-15}$	$(5.56 \pm 2.45) \times 10^{-18}$	$(1.34 \pm 0.59) \times 10^{-17}$
[O I] $\lambda$ 6300	190	$(1.42 \pm 0.73) \times 10^{-16}$	$(4.52 \pm 2.87) \times 10^{-19}$	$(8.68 \pm 5.51) \times 10^{-19}$
H $\alpha$	190	$(3.49 \pm 0.48) \times 10^{-15}$	$(1.07 \pm 0.15) \times 10^{-17}$	$(1.98 \pm 0.29) \times 10^{-17}$
[N II] $\lambda$ 6584	190	$(1.16 \pm 0.16) \times 10^{-15}$	$(3.46 \pm 0.50) \times 10^{-18}$	$(6.39 \pm 0.92) \times 10^{-18}$
[S II] $\lambda$ 6716	190	$(2.98 \pm 1.06) \times 10^{-16}$	$(8.43 \pm 3.49) \times 10^{-19}$	$(1.53 \pm 0.63) \times 10^{-18}$
[S II] $\lambda$ 6731	190	$(2.48 \pm 0.86) \times 10^{-16}$	$(7.65 \pm 3.17) \times 10^{-19}$	$(1.39 \pm 0.58) \times 10^{-18}$
<b>Broad Component</b>				
H $\beta$	705	$(3.34 \pm 1.02) \times 10^{-16a}$	$(8.89 \pm 3.31) \times 10^{-19a}$	$(2.20 \pm 0.82) \times 10^{-18a}$
[O III] $\lambda$ 5007	705	$(1.16 \pm 0.34) \times 10^{-15}$	$(3.87 \pm 1.70) \times 10^{-18}$	$(9.33 \pm 4.11) \times 10^{-18}$
[O I] $\lambda$ 6300	725	$(4.89 \pm 2.52) \times 10^{-16}$	$(1.18 \pm 0.75) \times 10^{-18}$	$(2.56 \pm 1.63) \times 10^{-18}$
H $\alpha$	725	$(1.33 \pm 0.18) \times 10^{-15}$	$(3.40 \pm 0.49) \times 10^{-18}$	$(6.30 \pm 0.91) \times 10^{-18}$
[N II] $\lambda$ 6584	725	$(1.72 \pm 0.24) \times 10^{-15}$	$(4.61 \pm 0.66) \times 10^{-18}$	$(8.50 \pm 1.22) \times 10^{-18}$
[S II] $\lambda$ 6716	725	$(2.76 \pm 0.99) \times 10^{-16b}$	$(8.84 \pm 3.66) \times 10^{-19b}$	$(1.61 \pm 0.67) \times 10^{-18b}$
[S II] $\lambda$ 6731	725	$(6.40 \pm 2.28) \times 10^{-16}$	$(1.72 \pm 0.71) \times 10^{-18}$	$(3.13 \pm 1.30) \times 10^{-18}$

**Notes.**

<sup>a</sup> Estimated assuming  $H\alpha_{\text{narrow}}/H\beta_{\text{narrow}} = H\alpha_{\text{broad}}/H\beta_{\text{broad}}$ .

<sup>b</sup>  $3\sigma$  detection flux limit.

detailed in Rigby et al. (2018). Comparable H $\alpha$  emission was obtained by binning SINFONI spaxels that overlap with locations of the strongest Ly $\alpha$  flux knots in the *HST* imaging (boxes in the flux map of Figure 6). The observed velocity structure of Ly $\alpha$  in comparison to Balmer emission is typical of studies of Green Pea galaxies (Yang et al. 2017; Orlitova et al. 2018). Although the sampled spectra are immediately adjacent to the detected AGN outflows, by fitting Gaussians to the binned H $\alpha$  spectrum we measure an FWHM of  $\sim 200$  km s<sup>-1</sup>, which suggests relatively undisturbed kinematics, and do not detect a secondary, outflow component. These observations suggest that the AGN outflows in SGAS 0033+02 are anticorrelated with the observed Ly $\alpha$  structure.

To estimate the intrinsic properties of the AGN in the source plane of SGAS 0033+02, we must apply a gravitational lens model to our observed image-plane data. Details of the methods used to convert image-plane observations of SGAS 0033+02 into source-plane data are detailed in the Appendix. From our model, we find that the main arc of SGAS 0033+02 straddles a lensing critical line, which separate regions of different image multiplicities. As such, the observed structure in this arc is approximately half of the galaxy observed in the counter images.

## 4. Source-plane Analysis

### 4.1. Extent of AGN Outflows

Figure 7 shows the source-plane reconstruction of the fraction of SGAS 0033+02 observed in the main arc as it would have been seen without the presence of the lens. Orange and green contours represent the source-plane extents of the narrow and broad H $\alpha$  emission-line components from SINFONI observations shown in Figure 3, respectively. Measuring the radial extent of the broad component (i.e., outflows) in the source plane, we report a length of  $r \sim 100$  pc. This is likely the maximum outflow extent in the observed half

of the galaxy, because the location of the outflows is adjacent to the rest-frame optical continuum peak of the galaxy in Figure 7, which suggests that they reside near the galaxy nucleus and AGN. However, this measurement should be treated as a lower limit to the true outflow extent, as we have no kinematic data on the other half of the galaxy that is not observed in the arc. We can measure the distance between the furthest knot of emission in the other half of the galaxy, as seen in the F555W image of Counter Image 1, which traces the extent of the observed H $\alpha$  emission, and its F140W continuum peak to set an upper limit on the maximum possible outflow distance as  $r \sim 830$  pc.

### 4.2. Intrinsic Flux Measurement

By reconstructing the source-plane image of SGAS 0033+02, we can also determine the magnification at any given point in the image plane. Demagnified fluxes for the AGN-ionized outflows in SGAS 0033+02 were obtained by dividing the image-plane data cubes by a magnification map at matched pixel-scale resolution, as determined from our strong lens model. Spectra in the central  $0''.5 \times 0''.5$  square were again binned and fit to measure the total demagnified flux. In this second iteration of fitting, line dispersions and centroids were fixed to the values obtained from the fit to the image-plane spectrum, with only the total flux (i.e., the Gaussian amplitude) allowed to vary. Source-plane fluxes are provided in Table 1.

Before analyzing our measured fluxes, we applied a reddening correction using a standard Galactic reddening curve (Savage & Mathis 1979) and color excesses calculated from the observed, source-plane H $\alpha$ /H $\beta$  ratio (Osterbrock & Ferland 2006), assuming an intrinsic recombination value of 2.85. The extinction was calculated using

$$E(B - V) = -\frac{2.5 \log\left(\frac{E_o}{F_i}\right)}{R_\lambda} = \frac{2.5 \log\left(\frac{(H\alpha/H\beta)_i}{(H\alpha/H\beta)_o}\right)}{R_{H\alpha} - R_{H\beta}}$$

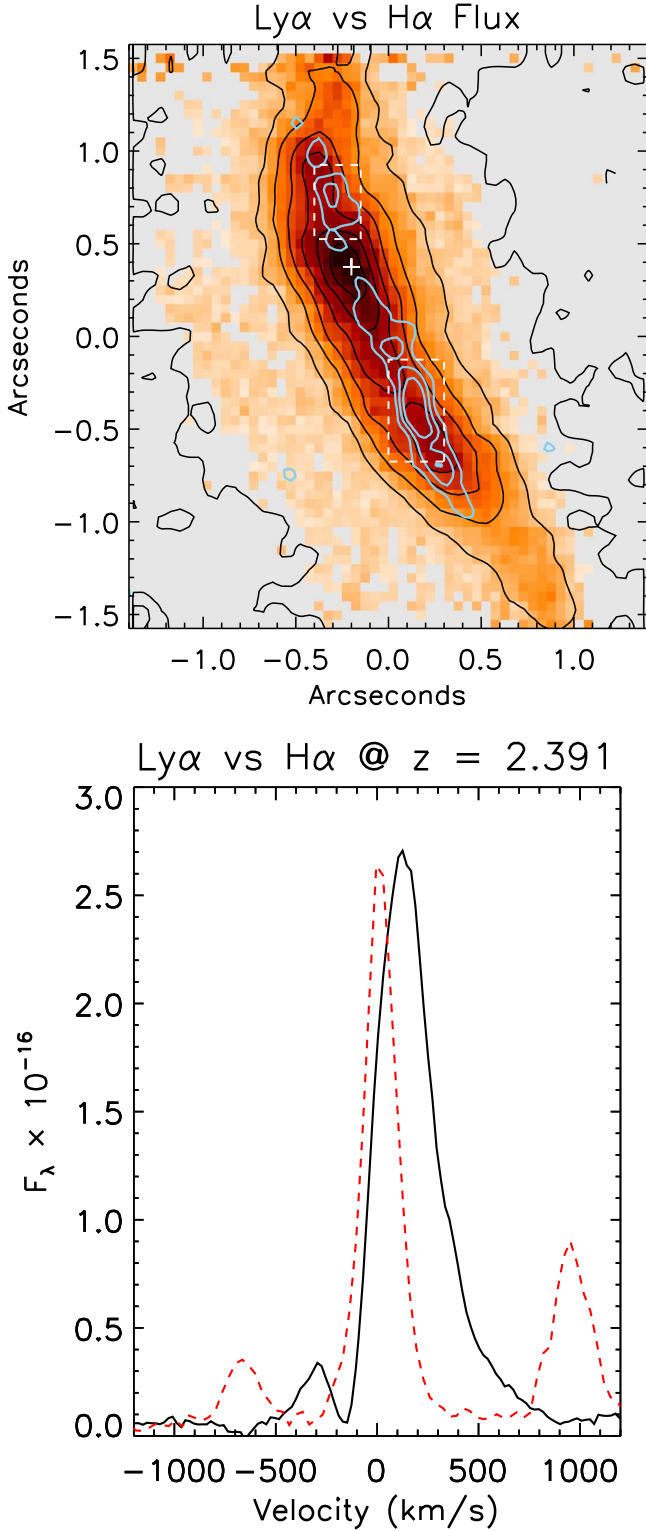


**Figure 6.** Top: integrated  $H\alpha$  flux map from SINFONI spectral fits with continuum-subtracted  $H\alpha$  flux contours in black and continuum-subtracted  $Ly\alpha$  flux contours in blue.  $Ly\alpha$  contour levels represent  $1\sigma$ ,  $2\sigma$ , and  $3\sigma$  fluxes above the background. White, dashed boxes show regions of SINFONI spaxels that were binned to measure  $H\alpha$  flux. Bottom: comparison of  $H\alpha + [N\ II] \lambda\lambda 6548, 6584$  (red dashed line) and  $Ly\alpha$  (black solid line) emission-line profiles, taken from SINFONI and MagE observations by Rigby et al. (2018), respectively.

where  $E(B - V)$  is the color excess,  $R_\lambda$  is the reddening value at a particular wavelength, and  $F_o$  and  $F_i$  are the observed and intrinsic fluxes, respectively. Galactic reddening values are

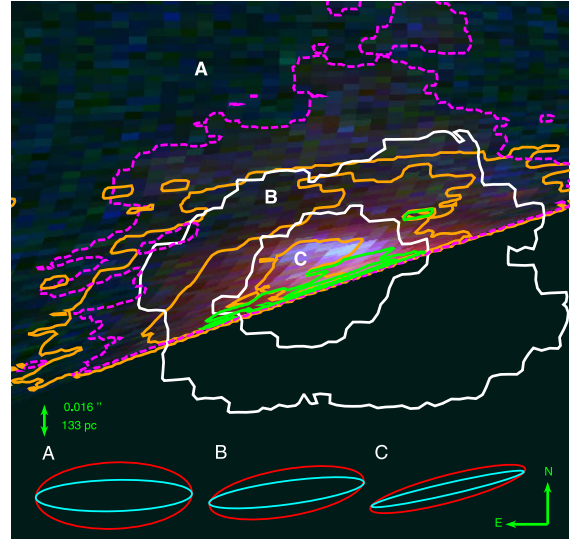


**Figure 7.** Source-plane reconstruction of *HST* F140W/F814W/F555W WFC3 imaging for the northern half of the main arc. Overplotted orange and green contours represent reconstructed narrow- and broad-component  $H\alpha$  fluxes from Figure 3, respectively. The magenta and white contours represent rest-frame optical continuum F140W image fluxes of the source-plane reconstruction for the arc and Counter Image 1, respectively. Source-plane images of the arc and counter image are aligned manually, because parametric modeling does not match the position in the source plane between images. Red and cyan ellipses below represent  $0''.140$  and  $0''.067$  circular PSF FWHMs for F140W and F555W filters, respectively, lensed back to the source plane. Ellipses are labeled with letters that map the transformation moving toward the caustic line.

$R_{H\alpha} \approx 2.5$  and  $R_{H\beta} \approx 3.7$ . Corrected line fluxes are then given by

$$F_i = \frac{10^{-0.4 R_\lambda E(B-V)}}{F_o}$$

with dereddened source-plane fluxes listed in Table 1.

#### 4.3. AGN Mass Outflow Rate

We use the dereddened source-plane flux of the broad  $H\alpha$  component to estimate the total, observed ionized gas mass in the NLR outflows, for case B recombination (Peterson 1997; Osterbrock & Ferland 2006). The total luminosity of  $H\beta$ , originating from clouds within a total volume  $V_c$ , is  $L(H\beta) = n_e n_p a_{H\beta}^{\text{eff}} h\nu_{H\beta} V_c$ , with  $a_{H\beta}^{\text{eff}}$  and  $\nu_{H\beta}$  being the effective recombination coefficient and rest frequency of  $H\beta$ , and  $n_e$  and  $n_p$  being the number densities of electrons and protons. We assume completely ionized hydrogen clouds, therefore  $n_e \sim n_p$ .  $H\alpha$  and  $H\beta$  luminosities are related such that  $L(H\alpha) = (j_{H\alpha}/j_{H\beta})L(H\beta)$ , where  $j_{H\alpha}/j_{H\beta}$  is the intensity of  $H\alpha$  relative to  $H\beta$ . Assuming the same density for all clouds,  $n_p m_p$ , with  $m_p$  being the proton mass, the total ionized gas mass is  $M_{\text{NLR}} = n_p m_p \times V_c$ . From the relations made above:

$$M_{\text{NLR}} = \frac{m_p L(H\alpha)}{n_e (j_{H\alpha}/j_{H\beta}) a_{H\beta}^{\text{eff}} h\nu_{H\beta}}$$

$$M_{\text{NLR}} = 2.523 \times 10^5 \times L_{42}(H\alpha) M_\odot$$

where  $L_{42}(H\alpha)$  is in units of  $10^{42} \text{ erg s}^{-1}$ . Intrinsic  $a_{H\beta}^{\text{eff}}$  and  $j_{H\alpha}/j_{H\beta}$  were taken from Osterbrock & Ferland (2006), assuming a temperature of  $T = 10^4 \text{ K}$ . We derive an electron density ( $n_e \text{ cm}^{-3}$ ) using an estimated  $[S\ II] \lambda\lambda 6716/6731$  line ratio for



the AGN-ionized broad-emission-line component (Allen 1979; Osterbrock & Ferland 2006). We measure a dereddened [S II]  $\lambda 6731$  broad-component flux of  $3.13 \times 10^{-18} \text{ erg s}^{-1} \text{ cm}^{-2}$ , do not detect a comparable broad [S II]  $\lambda 6716$  component, and instead use a flux of  $1.61 \times 10^{-18} \text{ erg s}^{-1} \text{ cm}^{-2}$  as an upper limit because this represents a dereddened  $3\sigma$  flux detection at this wavelength, assuming a similar line dispersion. These fluxes produce a maximum ratio  $\sim 0.5$ , from which we assume  $n_e \sim 10^4 \text{ cm}^{-3}$ . Using a luminosity distance of  $D_L = 6.071 \times 10^{28} \text{ cm}$  (Wright 2006), we measure the dereddened  $L(\text{H}\alpha)$  of the outflowing wind to be  $2.92 \times 10^{41} \text{ erg s}^{-1}$  in the source plane, and calculate a gas mass of  $M_{\text{NLR}} = 7.37 \times 10^4 M_\odot$ . This measurement is derived from a  $0''.5 \times 0''.5$  bin containing spectra from both sides of the critical line, so the reported value assumes similar fluxes on the side of the lensed system hidden by the lensing critical line. Using this gas mass, we then calculate the mass outflow rate in this region by dividing the total mass  $M$  by the time  $t$  it takes to travel across the extent over which we observe the outflows, where  $t = R/v$ . We assume a maximum outflow extent of  $\sim 100 \text{ pc}$ , as derived from the strong lens model. Observed radial velocities of the outflows are on the scale of tens of  $\text{km s}^{-1}$ , but these are likely compromised by projection effects. We instead use the maximum blueshifted velocity defined as half the full width at zero maximum, approximately the  $3\sigma$  velocity offset from the centroid of the broad  $\text{H}\alpha$  component measured in our binned spectrum as our deprojected velocity,  $v = 924 \text{ km s}^{-1}$ . Using these parameters, we measure a mass outflow rate of  $\dot{M} = 0.67 M_\odot \text{ yr}^{-1}$ . The power of the outflow  $dE/dt$  is then calculated as

$$\frac{dE}{dt} = 0.5 \frac{Mv^2}{t}$$

for  $\log(\dot{E}/\text{erg s}^{-1}) = 41.33$ . We use the dereddened source-plane flux of the [O III]  $\lambda 5007$  and [O I]  $\lambda 6300$  broad components to measure the bolometric luminosity of the AGN, using the method from Netzer (2009),  $\log(L_{\text{bol}}) = 3.8 + 0.25 \log L([\text{O III}] \lambda 5007) + 0.75 \log L([\text{O I}] \lambda 6300)$ , for  $\log(L_{\text{bol}}/\text{erg s}^{-1}) = 45.02$ . The resulting ratio of outflow power to bolometric luminosity is  $\log(\dot{E}/L_{\text{bol}}) = -3.76$ , less than the 0.5% threshold typically required to provide a significant impact on the host galaxy (Hopkins & Elvis 2010).

#### 4.4. SFR

We convert the narrow-line, non-AGN-ionized  $\text{H}\alpha$  luminosity not attributed to AGN ionization (i.e., the  $\text{H}\alpha$  flux measured in the left column of Figure 3) to an SFR by using the relation from Kennicutt (1998), where  $\text{SFR}(M_\odot \text{ yr}^{-1}) = 7.9 \times 10^{-42} L(\text{H}\alpha)$ , and adjusting to the initial mass function from Chabrier (2003), which reduces the SFR by a factor of 1.7. We measure source-plane  $\text{H}\alpha$  luminosities north and south of the lensing caustic to be  $L(\text{H}\alpha)_{\text{north}} = 4.9 \times 10^{42} \text{ erg s}^{-1}$  and  $L(\text{H}\alpha)_{\text{south}} = 1.5 \times 10^{43} \text{ erg s}^{-1}$ , which convert to SFRs of  $22.8 M_\odot \text{ yr}^{-1}$  and  $70.7 M_\odot \text{ yr}^{-1}$ , respectively. We note that these rates may be upper limits, because there may be contributions to the H II regions from AGN ionization. We can compare our SFR measurements to those in Livermore et al. (2015), which show a correlation between SFR in star-forming

clumps and their sizes, by isolating a lower-limit SFR in the discrete, fully imaged  $\text{H}\alpha$  knot north of the continuum peak, as shown in Figures 3 and 6. Here, we measure a demagnified  $F(\text{H}\alpha) = 1.132 \times 10^{-17} \text{ erg s}^{-1} \text{ cm}^{-2}$ , which converts to an SFR of  $2.43 M_\odot \text{ yr}^{-1}$ , over an area of  $0.7 \text{ mas}^2$  in the source plane (Figure 7) for an approximate radius of  $15 \text{ mas}$ , or  $125 \text{ pc}$ . Measurements for the global SFR and the clump SFR both exceed the mass outflow rate of the AGN. Therefore, the central AGN, in its current state, is incapable of displacing enough material to quench star formation in this galaxy.

## 5. Discussion

Producing this spatially resolved analysis of AGN outflows in a “normal” star-forming galaxy at  $z \sim 2$ , we find it to be similar to weak AGNs with strong star formation in the nearby universe. The measured source-plane bolometric luminosity of this object suggests that we are observing a Seyfert-like AGN in SGAS 0033+02. In addition, the observed recombination emission-line dispersions indicate that SGAS 0033+02 is a Type 2 AGN, where the central engine is obscured along our line of sight. With the observed morphology of the bright, outflowing NLR being relatively compact, we find this target to be analogous to the nearby Seyfert 2 NGC 1068 (Crenshaw & Kraemer 2000; Das et al. 2006). From *HST* WFPC2 [O III] imaging (Schmitt et al. 2003), the enclosed [O III] flux within a  $100 \text{ pc}$  radius of the nucleus for this nearby AGN is  $9.11 \times 10^{-12} \text{ erg s}^{-1} \text{ cm}^{-2}$ , which converts to a luminosity of  $L([\text{O III}]) = 1.7 \times 10^{41} \text{ erg s}^{-1}$ . The measured flux in this system originates from one half of the NLR, with the other half extinguished below the plane of its host disk. For comparison, we can divide the measured  $L([\text{O III}])$  of SGAS 0033+02 of  $4.32 \times 10^{41} \text{ erg s}^{-1}$  in half and find its luminosity to be on par with NGC 1068 at  $L([\text{O III}]) = 2.16 \times 10^{41} \text{ erg s}^{-1}$ . Notably, as a Seyfert AGN with intrinsic observed  $F([\text{O III}]) = 3.87 \times 10^{-18} \text{ erg s}^{-1} \text{ cm}^{-2}$ , it is unlikely that the broad emission-line component attributed to AGN ionization in SGAS 0033+02 would be detected in a typical field galaxy at  $z = 2.391$ . Combined with the effects of the dilution of star formation hiding narrow AGN NLR signatures near systemic velocity, these findings suggest that many AGNs may go undetected in surveys of galaxies residing near Cosmic Noon (Trump et al. 2015).

There is no evidence in our current observations that we are missing broad outflowing emission-line components at greater radii due to lesser amounts of magnification. As shown in Figure 6, binning  $\text{H}\alpha$  lines exterior to where we detect AGN outflows results in a single Gaussian fit without the presence of a second, broad component. However, it remains unclear whether we are observing the true extent of the AGN outflows because, as described above, the main arc of SGAS 0033+02 is a partial image that contains roughly half of the galaxy seen in the counter images. Assuming that the outflows originate from the optical continuum peak, we cannot know the extent of the winds in the other half of the system without kinematics measurements for one of the counter images.

Comparing the extent of the AGN-ionized region to the AGN [O III] luminosity of SGAS 0033+02, we find that it has a relatively small extent for its luminosity when compared to the correlation of radius with luminosity for NLRs found in previous studies (Schmitt et al. 2003; Liu et al. 2010; Dempsey & Zakamska 2018; Fischer et al. 2018). Although we are likely observing the maximum extent of the AGN outflows in our

observations, a narrow AGN-ionized emission-line component displaying rotation kinematics that extends to larger distances would be undetected due to dilution by the larger flux contribution of the H II star-forming region. Measuring the source-plane radial extent of the [O III] emission shown in Figure 3, we find a maximum  $R_{[\text{O III}]} \sim 800$  pc. Assuming an AGN-ionized component exists throughout, a radial extent of 800 pc paired with  $\log(L[\text{O III}]) = 41.6 \text{ erg s}^{-1}$  places SGAS 0033+02 in line with previous findings from Seyferts and QSOs in the nearby universe.

## 6. Conclusions

We have analyzed spatially resolved, rest-frame UV/optical imaging and spectroscopy of a Seyfert AGN at  $z \sim 2$  for the first time. Our major findings are:

(1) AGN-ionized outflows extend to a radius of  $r \sim 100$  pc. We calculate a mass outflow rate over this distance of  $\dot{M} = 0.55 M_{\odot} \text{ yr}^{-1}$ . The corresponding ratio of outflow power to bolometric luminosity is exceedingly low,  $\log(\dot{E}/L_{\text{bol}}) = -3.76$ , suggesting that the AGN does not significantly impact the host galaxy.

(2) SGAS 0033+02 also exhibits an SFR of the order of tens of solar masses per year, which greatly exceeds the AGN mass outflow rate. As such, the current state of the AGN in SGAS 0033+02 would be unlikely to quench star formation within the galaxy.

(3) The positions of outflowing winds and Ly $\alpha$  emission are anticorrelated. Ly $\alpha$  exists where the outflow is not, therefore the outflow has not destroyed Ly $\alpha$  over the whole arc. Ly $\alpha$  structure in this galaxy is also similar to that in galaxies not hosting AGNs.

(4) SGAS 0033+02 resembles weak AGNs with strong star formation observed in the local universe. Faint emission-line signatures of these low-luminosity AGNs make their detection at  $z \sim 2$  extremely difficult without gravitational lensing. Combining faint AGN emission with line-dilution from strong star formation, it is possible that many AGNs are missed in survey work at this redshift.

Based on observations collected at the European Organisation for Astronomical Research in the Southern Hemisphere under ESO programmes 094.A-0746(A) and 098.A-0459(A).

Based on observations made with the NASA/ESA *Hubble Space Telescope*, obtained from the data archive at the Space Telescope Science Institute. STScI is operated by the Association of Universities for Research in Astronomy, Inc. under NASA contract NAS 5-26555.

This paper includes data gathered with the 6.5 meter Magellan Telescopes located at Las Campanas Observatory, Chile.

The authors would like to thank the anonymous referee for their helpful comments. This paper benefited from discussions with D. M. Crenshaw, M. Revalski, and C. L. Gnilka. T.C.F. was supported by an appointment to the NASA Postdoctoral Program at the NASA Goddard Space Flight Center, administered by Universities Space Research Association under contract with NASA. S.L. was partially funded by UCh/VID project ENL18/18. L.F.B. was supported by Anillo ACT-1417.

## Appendix Gravitational Lens Modeling

### A.1. Methodology for Models of Lensing Mass

Here, we provide a brief summary of the gravitational lensing analysis used in this work and we refer the reader to Kneib et al. (1996), Smith et al. (2005), Richard et al. (2011), and Verdugo et al. (2011) for a more in-depth description. We take a parametric approach, using *Lenstool* (Jullo et al. 2007) to model the cluster mass distribution surrounding our target as a series of dual pseudo-isothermal ellipsoids (dPIEs, Elíasdóttir et al. 2007), which are optimized through a Monte Carlo Markov chain minimization.

To model the cluster mass distribution, dark matter (hereafter DM) dPIE clumps are combined to map the DM at the cluster scale. Galaxy-scale DM potentials are used to describe galaxy-scale substructure. Considering the large number of galaxies in the cluster, it is not feasible to optimize the parameters of every potential, because the large parameter space will lead to an unconstrained minimization. Moreover, hutching individual galaxies contribute only a small fraction to the total mass budget of the cluster, so their effects on lensing are minimal unless they are in close proximity, in projection, to the lensed galaxies. To reduce the overall parameter space we scale the parameters of each galaxy to a reference value, using a constant mass–luminosity scaling relation (see Limousin et al. 2007).

### A.2. Selection of Cluster Members

We used SExtractor in the “white” image of the MUSE data to detect all the sources and define apertures for PyMuse (<https://pypi.org/project/PyMUSE/>) to integrate the spaxels and thus to obtain the spectra for each of the galaxies. PyMuse can also run Redmonster (Hutchinson et al. 2016) to determine individual redshifts. All the spectra, and Redmonster best candidates, were visually inspected to assign the redshift for each galaxy.

We then constructed a galaxy cluster catalog using the red sequence technique (Gladders & Yee 2000), by selecting in a color–magnitude diagram galaxies that show a similar color. Our final catalog contains 80 cluster members.

The brightest galaxies, or bright cluster galaxies (BCGs), of galaxy clusters tend to not follow the cluster red sequence, so we remove the BCG of the southeast subcluster (Newman et al. 2013a, 2013b). We keep the other BCGs in the scaling relation because of the lack of constraints to properly model the shape of the lensing potential on that side. In addition, we detected several spiral galaxies in the MUSE data cube at  $z \sim 1.03$  (L. F. Barrientos et al. 2019, in preparation) that may influence the lensing configuration of the bright arc of SGAS 0033+02. We include the two closest ones ( $\alpha = 00^{\text{h}}33^{\text{m}}41^{\text{s}}.6576$ ,  $\delta = +02^{\circ}42'13''.7186$  and  $\alpha = 00^{\text{h}}33^{\text{m}}41^{\text{s}}.0841$ ,  $\delta = +02^{\circ}42'05''.5126$ ) in our lensing potentials, but model them separately as individual potentials at the cluster redshift.

### A.3. Lensing Constraints

We consider a large number of constraints for the bright arc in order to obtain the most accurate source reconstructions. Figure 8 exhibits an *HST* F555W/F814W/F140W image



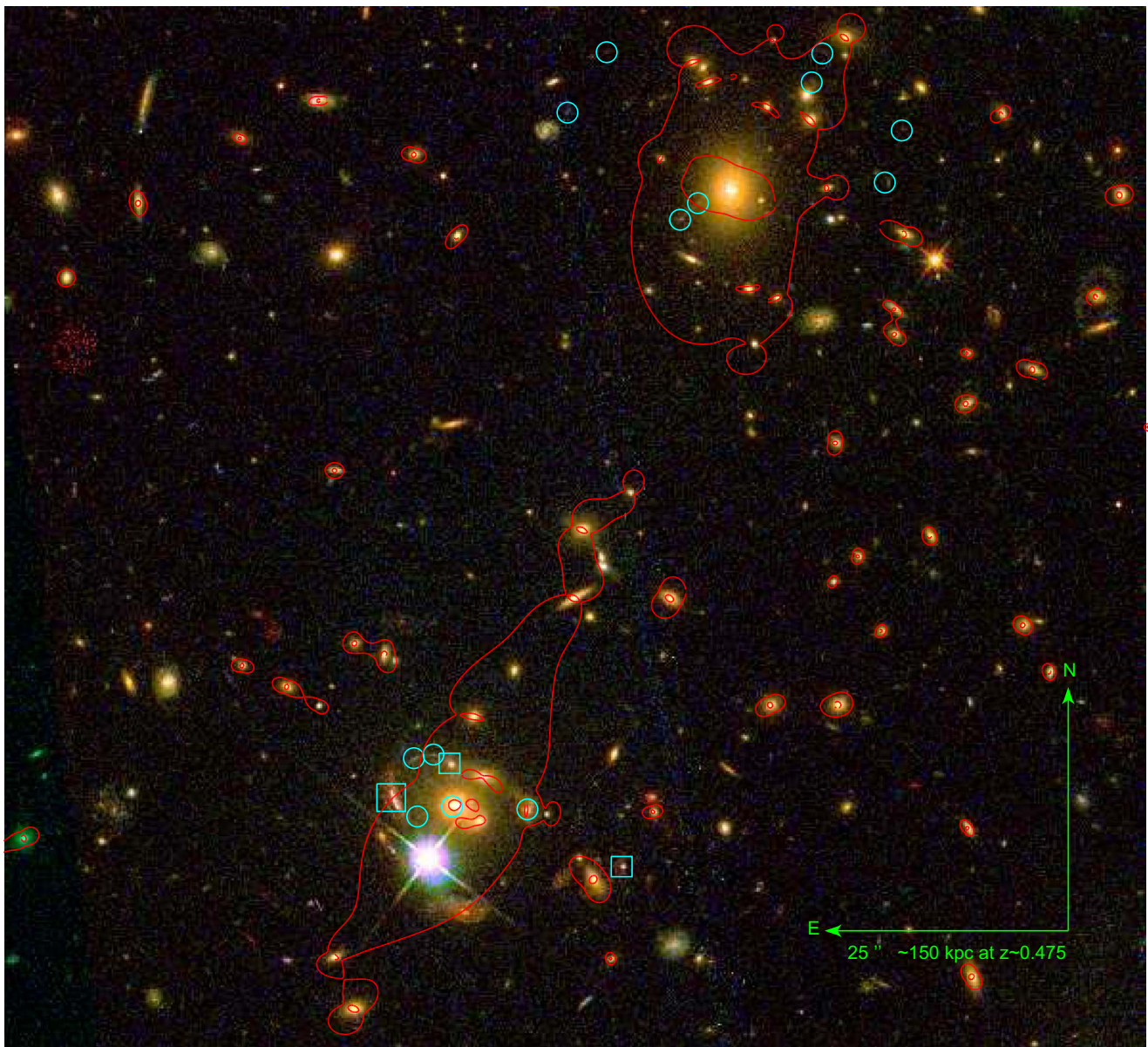


**Figure 8.** *HST* F555W/F814W/F140W image detailing the locations of all the strong lensing observed in the field. The red curve is the critical line at  $z = 2.39$ , the redshift of SGAS 0033+02. Cyan circles are constraints used in the model. Cyan squares are the region where the SGAS 0033+02 constraints are positioned.



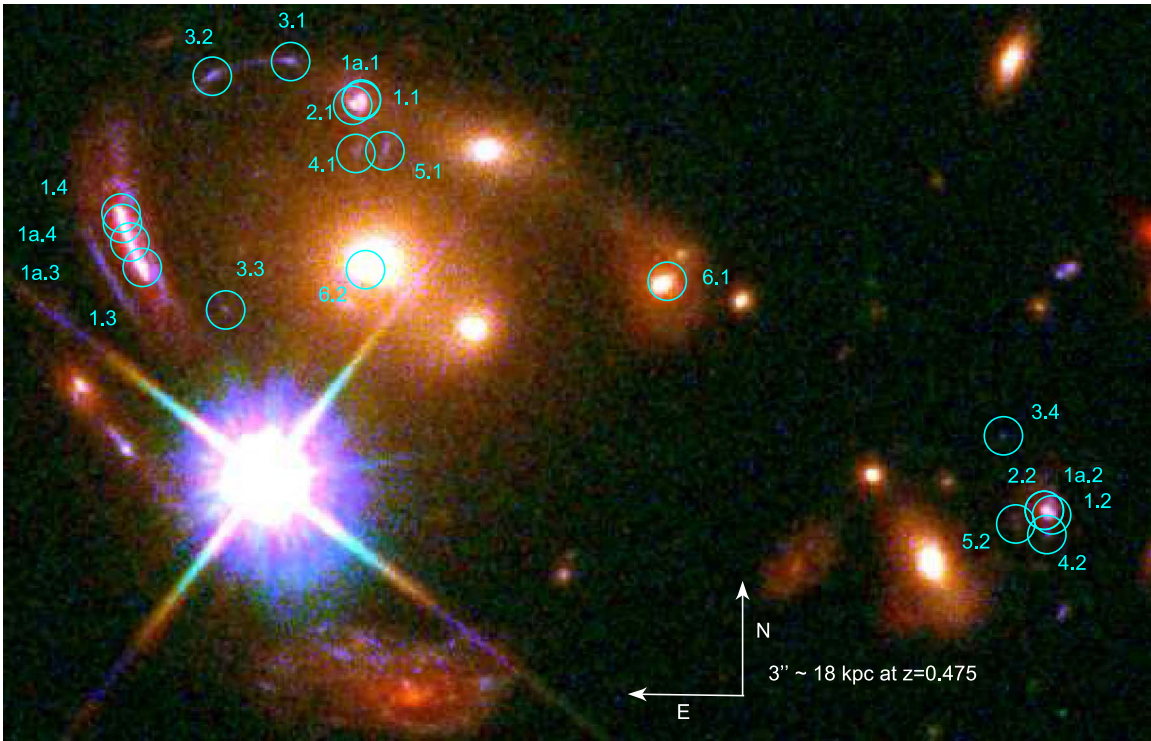


**Figure 9.** Enlargement of the southern cluster in Figure 8, identifying individual constraints in the lensing model as cyan circles. Systems 1 and 1a are almost overlapping, see Table 2 for more information.

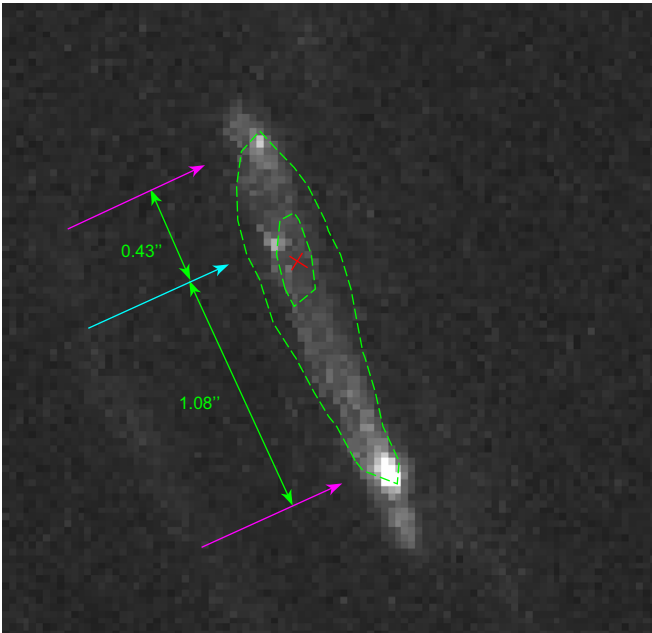


**Figure 10.** *HST* F555W image showing the asymmetry in the SGAS 0033+02 arc morphology. The green dashed contour shows the luminosity contour of the F140W *HST* band. The red cross shows the rest-frame optical continuum peak and expected crossing of the critical curve. The two magenta arrows show the two bright knots that are identified as being the same emission knot on either side of the critical line. The cyan arrow marks the bright spot that does not have a symmetrical counterpart.

marking the positions of all constraints used in our model and the resultant critical line. We also provide an enlarged, labeled image of the region near SGAS 0033+02 in Figure 9, with the positions and redshifts of these systems listed in Table 2. From our model, we find that the lensing critical line at  $z = 2.39$  lies directly over the center of the arc of SGAS 0033+02, such that the north and south ends of the arc are reflections of one another. This is supported by the symmetries on each side of the arc observed in both imaging and kinematics.

We find that the arc contains an unusual asymmetry that cannot be accounted for by the lensing model, observed in the rest-frame UV continuum F555W image, as shown in Figure 10. As the critical line from the strong lensing model crosses at the flux peak in the F140W image, as shown in Figure 11, we observe that the small and faint emission knot just north of the critical curve does not show a symmetric counterpart on the other side of the arc. As such, this emission could be due to a transient in the arc and we do not include this feature in our constraints. In addition, the southern emission knot in the F555W image is significantly brighter than the corresponding knot in the top arc. This knot coincides with the  $H\alpha$  knot visible in SINFONI data (see Figure 3), which also show this flux asymmetry. A possible explanation of this discrepancy is that the observed flux of this feature varies in time, but additional observations are required to test such a scenario.

**Table 2**  
Lensing Constraints

ID	$\Delta\alpha^a$ (h:m:s)	$\Delta\delta^a$ (d:m:s)	$z_{\text{spec}}^b$	$z_{\text{model}}^c$ (arcsec)	rms <sup>d</sup>
1.1	0:33:41.167	+2:42:21.200	2.39	...	0.15
1.2	00:33:39.977	+02:42:10.4602	2.39	...	0.08
1.3	00:33:41.549	+02:42:16.802	2.39	...	0.20
1.4	00:33:41.586	+02:42:18.223	2.39	...	0.13
1a.1	00:33:41.167	+02:42:21.1589	2.39	...	0.14
1a.2	00:33:39.9765	+02:42:10.4568	2.39	...	0.08
1a.3	00:33:41.5704	+02:42:17.4662	2.39	...	0.09
1a.4	00:33:41.5835	+02:42:17.9503	2.39	...	0.09
2.1	00:33:41.1822	+02:42:21.0352	2.39	...	0.09
2.2	00:33:39.964	+02:42:10.3392	2.39	...	0.15
3.1	00:33:41.2903	+02:42:22.1782	2.096	...	0.35
3.2	00:33:41.4269	+02:42:21.7955	2.096	...	0.05
3.3	00:33:41.4035	+02:42:15.6917	2.096	...	0.46
3.4	00:33:40.048	+02:42:12.4045	2.096	...	0.05
4.1	00:33:41.1767	+02:42:19.7782	2.39	...	0.05
4.2	00:33:39.9723	+02:42:09.8256	2.39	...	0.09
5.1	00:33:41.126	+02:42:19.845	2.39	...	0.11
5.2	00:33:40.0265	+02:42:10.1024	2.39	...	0.30
6.1	00:33:40.634	+02:42:16.441	0.969	...	0.04
6.2	00:33:41.1598	+02:42:16.7427	0.969	...	0.10
7.1	00:33:38.019	+02:43:27.487	...	$5.70^{+0.69}_{-0.54}$	0.12
7.2	00:33:38.574	+02:43:35.552	...	$5.70^{+0.69}_{-0.54}$	0.36
7.3	00:33:40.08	+02:43:35.6793	...	$5.70^{+0.69}_{-0.54}$	0.21
8.1	00:33:39.4425	+02:43:19.8843	...	$5.72^{+2.03}_{-0.09}$	0.06
8.2	00:33:39.5671	+02:43:18.1456	...	$5.72^{+2.03}_{-0.09}$	0.05
9.1	00:33:38.137	+02:43:22.043	...	$3.92^{+0.32}_{-0.34}$	0.09
9.2	00:33:38.648	+02:43:32.52	...	$3.92^{+0.32}_{-0.34}$	0.11
9.3	00:33:40.3541	+02:43:29.3617	...	$3.92^{+0.32}_{-0.34}$	0.06

**Notes.**

<sup>a</sup>  $\Delta\alpha$  and  $\Delta\delta$  are the position of the arc.

<sup>b</sup>  $z_{\text{spec}}$  refers to the spectroscopic redshift set to the arc; when no value is present we let the redshift be free to vary during the minimization.

<sup>c</sup>  $z_{\text{model}}$  refers to the best redshift found by our modelisation.

<sup>d</sup> rms refers to the square root of the mean square of the predicted image position and represents the goodness of our fiducial model regarding the position of each constraint.

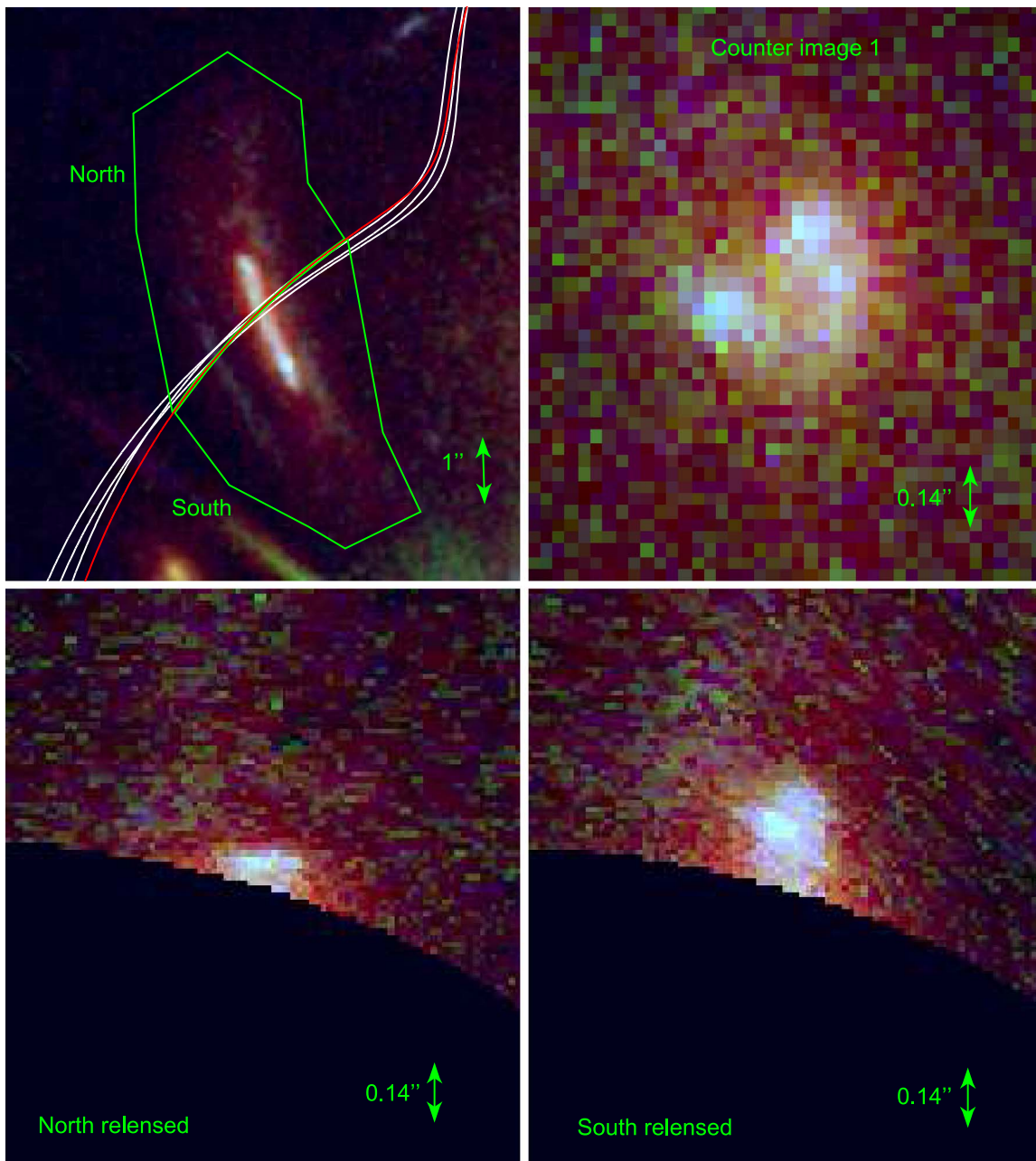


**Figure 11.** Top: enlargement of Figure 8 centered on the main arc (left) and Counter Image 1 (right) of SGAS 0033+02. The main arc image of SGAS 0033+02 shows the location of the critical line of our lensing model and green polygon regions north and south of the critical line, which are used to produce the reconstructed source-plane images. Bottom left: the released image of the north bin from the top left image matched to the position of Counter Image 1. Bottom right: the released image of the south bin from the top left image matched to the position of Counter Image 1.

### ORCID iDs

Travis C. Fischer <https://orcid.org/0000-0002-3365-8875>  
 G. Mahler <https://orcid.org/0000-0003-3266-2001>  
 K. Sharon <https://orcid.org/0000-0002-7559-0864>  
 M. Florian <https://orcid.org/0000-0001-5097-6755>  
 M. Bayliss <https://orcid.org/0000-0003-1074-4807>  
 H. Dahle <https://orcid.org/0000-0003-2200-5606>  
 E. Wuyts <https://orcid.org/0000-0002-4105-3315>

### References

Abuter, R., Schreiber, J., Eisenhauer, F., et al. 2006, *NewAR*, **50**, 398  
 Allen, D. A. 1979, *MNRAS*, **186**, 1

Baldwin, J. A., Phillips, M. M., & Terlevich, R. 1981, *PASP*, **93**, 5  
 Bayliss, M. B., Sharon, K., Ayan, A., et al. 2017, *ApJL*, **845**, L14  
 Brusa, M., Cresci, G., Schramm, M., et al. 2016, *A&A*, **588**, A58  
 Buchner, J., Georgakakis, A., Nandra, K., et al. 2014, *A&A*, **564**, A125  
 Carniani, S., Marconi, A., Maiolino, R., et al. 2015, *A&A*, **580**, A102  
 Chabrier, G. 2003, *PASP*, **115**, 763  
 Crenshaw, D. M., & Kraemer, S. B. 2000, *ApJ*, **532**, 247  
 Cresci, G., Mainieri, V., Brusa, M., et al. 2015, *ApJ*, **799**, 82  
 Das, V., Crenshaw, D. M., Kraemer, S. B., & Deo, R. P. 2006, *AJ*, **132**, 620  
 Davé, R., Finlator, K., & Oppenheimer, B. D. 2012, *MNRAS*, **421**, 98  
 Dempsey, R., & Zakamska, N. L. 2018, *MNRAS*, **477**, 4615  
 Elíasdóttir, Á., Limousin, M., Richard, J., et al. 2007, arXiv:0710.5636  
 Fabian, A. C. 2012, *ARA&A*, **50**, 455  
 Feroz, F., & Hobson, M. P. 2008, *MNRAS*, **384**, 449  
 Feroz, F., Hobson, M. P., & Bridges, M. 2009, *MNRAS*, **398**, 1601  
 Feroz, F., Hobson, M. P., Cameron, E., & Pettitt, A. N. 2013, arXiv:1306.2144



- Fischer, T. C., Kraemer, S. B., Schmitt, H. R., et al. 2018, *ApJ*, **856**, 102
- Fischer, T. C., Machuca, C., Diniz, M. R., et al. 2017, *ApJ*, **834**, 30
- Förster Schreiber, N. M., Genzel, R., Bouché, N., et al. 2009, *ApJ*, **706**, 1364
- Förster Schreiber, N. M., Genzel, R., Newman, S. F., et al. 2014, *ApJ*, **787**, 38
- Förster Schreiber, N. M., Renzini, A., Mancini, C., et al. 2018, *ApJS*, **238**, 21
- Genzel, R., Förster Schreiber, N. M., Rosario, D., et al. 2014, *ApJ*, **796**, 7
- Gladders, M. D., & Yee, H. K. C. 2000, *AJ*, **120**, 2148
- Hayes, M., Östlin, G., Schaerer, D., et al. 2013, *ApJL*, **765**, L27
- Hopkins, P. F., & Elvis, M. 2010, *MNRAS*, **401**, 7
- Hutchinson, T. A., Bolton, A. S., Dawson, K. S., et al. 2016, *AJ*, **152**, 205
- Jullo, E., Kneib, J.-P., Limousin, M., et al. 2007, *NJPh*, **9**, 447
- Karouzos, M., Woo, J.-H., & Bae, H.-J. 2016, *ApJ*, **819**, 148
- Keel, W. C., Lintott, C. J., Maksym, W. P., et al. 2017, *ApJ*, **835**, 256
- Kennicutt, R. C. J. 1998, *ARA&A*, **36**, 189
- Kewley, L. J., Maier, C., Yabe, K., et al. 2013, *ApJL*, **774**, L10
- Kneib, J.-P., Ellis, R. S., Smail, I., Couch, W. J., & Sharples, R. M. 1996, *ApJ*, **471**, 643
- Limousin, M., Richard, J., Jullo, E., et al. 2007, *ApJ*, **668**, 643
- Liu, X., Greene, J. E., Shen, Y., & Strauss, M. A. 2010, *ApJL*, **715**, L30
- Livermore, R. C., Jones, T. A., Richard, J., et al. 2015, *MNRAS*, **450**, 1812
- Nesvadba, N. P. H., Drouart, G., De Breuck, C., et al. 2017, *A&A*, **600**, A121
- Nesvadba, N. P. H., Lehnert, M. D., De Breuck, C., Gilbert, A. M., & van Breugel, W. 2008, *A&A*, **491**, 407
- Nesvadba, N. P. H., Polletta, M., Lehnert, M. D., et al. 2011, *MNRAS*, **415**, 2359
- Netzer, H. 2009, *MNRAS*, **399**, 1907
- Newman, A. B., Treu, T., Ellis, R. S., et al. 2013b, *ApJ*, **765**, 24
- Newman, A. B., Treu, T., Ellis, R. S., & Sand, D. J. 2013a, *ApJ*, **765**, 25
- Orlitova, I., Verhamme, A., Henry, A., et al. 2018, arXiv:1806.01027
- Osterbrock, D. E., & Ferland, G. J. 2006, *Astrophysics of Gaseous Nebulae and Active Galactic Nuclei* (Sausalito, CA: Univ. Science Books)
- Östlin, G., Hayes, M., Kunth, D., et al. 2009, *AJ*, **138**, 923
- Perna, M., Brusa, M., Salvato, M., et al. 2015, *A&A*, **583**, A72
- Peterson, B. M. 1997, *An Introduction to Active Galactic Nuclei* (Cambridge: Cambridge Univ. Press)
- Ramos Almeida, C., Piqueras López, J., Villar-Martín, M., & Bessiere, P. S. 2017, *MNRAS*, **470**, 964
- Richard, J., Kneib, J.-P., Ebeling, H., et al. 2011, *MNRAS*, **414**, L31
- Rigby, J. R., Bayliss, M. B., Sharon, K., et al. 2018, *AJ*, **155**, 104
- Savage, B. D., & Mathis, J. S. 1979, *ARA&A*, **17**, 73
- Schmitt, H. R., Donley, J. L., Antonucci, R. R. J., Hutchings, J. B., & Kinney, A. L. 2003, *ApJS*, **148**, 327
- Schreiber, J., Thatte, N., Eisenhauer, F., et al. 2004, in ASP Conf. Ser. 314, *Astronomical Data Analysis Software and Systems (ADASS) XIII*, ed. F. Ochsenbein, M. G. Allen, & D. Egret (San Francisco, CA: ASP), 380
- Smith, G. P., Kneib, J.-P., Smail, I., et al. 2005, *MNRAS*, **359**, 417
- Trump, J. R., Sun, M., Zeimann, G. R., et al. 2015, *ApJ*, **811**, 26
- Verdugo, T., Motta, V., Muñoz, R. P., et al. 2011, *A&A*, **527**, A124
- Villar-Martín, M., Arribas, S., Emonts, B., et al. 2016, *MNRAS*, **460**, 130
- Vogelsberger, M., Genel, S., Sijacki, D., et al. 2013, *MNRAS*, **436**, 3031
- Wright, E. L. 2006, *PASP*, **118**, 1711
- Yang, H., Malhotra, S., Gronke, M., et al. 2017, *ApJ*, **844**, 171